Hollow cathode thermal modelling and self-consistent plasma solution: work function evaluation for a LaB_6 cathode.

Pablo Guerrero *
California Institute of Technology, Pasadena, CA, 91125

Ioannis G. Mikellides † and James E. Polk ‡
Jet Propulsion Laboratory, California Institute of Technology, Pasadena, CA, 91109

Daniel I. Meiron§
California Institute of Technology, Pasadena, CA, 91125

Self-heating hollow cathodes are central components in modern electric thrusters. The plasma discharge inside these devices heats the internal components, thus maintaining the temperatures required for electron emission. Precise knowledge of the physical phenomena governing hollow cathode operation is key to predict their lifetime, specifically, their thermionic emission characteristics. A simulation platform has been built to couple plasma and thermal models of the self-heating hollow cathode to produce a self-consistent solution. A self-consistent solution has been found for a LaB_6 hollow cathode operating at 25A and 13 sccm where the work function is assumed to be spatially uniform along the emitter with a value which is allowed to vary as the coupled model iterates to a self-consistent solution. The emitter temperature from the converged solution does not agree with experimental temperature measurements, however. The results of a sensitivity analysis suggest that none of the tolerances in the measurement are responsible for the discrepancy. We hypothesize that either the work function needs to be a function of position along the emitting surfaces or the heat fluxes have been overestimated in the plasma solver.

Nomenclature

J_D	=	Net discharge current
V_D	=	Discharge voltage
j_{ther}	=	Thermionic emission density
T	=	Temperature
ε	=	Total hemispherical emissivity
$\dot{m}_{Xe}$	=	Xenon mass flow rate
ϕ	=	work function
$\phi_{Schottky}$	=	Modification of the work function due to the Schottky effect
$\bar{z}$	=	Dimensional coordinate along centerline of the cathode
$T_{insert}(z)$	=	Temperature distribution along the hollow cathode insert
V_K	=	Keeper voltage
e	=	Electron charge
k_B	=	Boltzmann constant
D	=	Richardson-Dushman law constant

*PhD Candidate, Galcit, Caltech, 1200 E California Blvd, Pasadena, CA 91125, AIAA student Member

†Principal Engineer, Electric Propulsion Group, Jet Propulsion Laboratory, California Institute of Technology, M/S 125-109, 4800 Oak Grove Drive, Pasadena, CA 91109. Associate Fellow AIAA

‡Principal Engineer, Propulsion and Materials Engineering Section, Jet Propulsion Laboratory, California Institute of Technology, M/S 125-109, 4800 Oak Grove Drive, Pasadena, CA 91109. Associate Fellow AIAA

§Fletcher Jones Professor of Aeronautics and Applied and Computational Mathematics, Graduate Aerospace Laboratories, California Institute of Technology, Pasadena, Ca, 91125

I. Introduction

Reaching further, going faster and delivering heavier payloads are the ultimate goals of the design of any space vehicle. In order to improve the current technical capabilities and enable more ambitious deep space missions, NASA is investing in high power electric propulsion systems. Scalable arrays of Hall thrusters are at the heart of these propulsion systems.

Hollow cathodes are among the basic components necessary for Hall thruster operation, and therefore cathode lifetime is a major determinant of thruster lifetime. There are several cathode failure processes which are still not fully understood and a better understanding of the different physical mechanisms that govern cathode discharges is necessary. Thermionic emission of electrons is the most fundamental mechanism of cathode discharge. Thermionic emission is tightly dependent on the work function of the emitting surface of the cathode. Cathodes composed of a porous tungsten emitter impregnated with barium-calcium-aluminate mixture are the baseline for the Advanced Electric Propulsion System (AEPS) that is under development by the NASA Glenn Research Center (GRC) and the Jet Propulsion Laboratory (JPL) with Aerojet Rocketdyne as an industrial partner. This technology maintains a relatively low work function during the operation of the cathode, conferring a long lifetime. LaB_6 cathodes are a promising alternative with several advantages over tungsten cathodes, which include emitting surface oxides self-cleaning, greater resilience to contamination, and low work function. A low work function is beneficial for electron emitters because it enables operation at a lower temperature for a given emission current, which reduces the evaporation of the emitting material and thus increases their useful lifetime.

Hollow cathodes are thermionic emitters classically modelled with the Dushman-Richardson law (Eq. 1) [1]. This law relates temperature, emission current density of electrons and work function. Several phenomena must be taken into account when studying the emission characteristic of a hollow cathode, namely 1) the return current of electrons and ions to the emitting surface, 2) the Schottky effect, 3) space charge limitations, 4) temperature variation along the emitting surfaces and 5) work function variation due to evolution of the chemistry and/or crystallographic structure of the emitting surfaces.

$$j_{ther}(\phi, T) = DT^2 \exp\left(\frac{-e(\phi - \phi_{Schottky})}{k_B T}\right) \tag{1}$$

Where T is the temperature at the emitting surface, $D = 29A/cm^2K^2$ to account for the work function temperature dependency, k_B is the Boltzmann constant, ϕ is the work function of the material, $\phi_{Schottky}$ is the reduction in the work function due to the external electric field and e is the electron charge.

In order to illustrate the thermionic behavior of a cathode, a simple analysis can be done by assuming the following simplifications:

1) No net return current (contribution from plasma electrons and ions)
2) $\phi_{Schottky} = 0$
3) Current is not space charge limited
4) Uniform temperature along the emitter
5) Uniform work function along the emitter

Fig. 1 shows a study of thermionic emission current density with temperature and ϕ as a parameter for a range of temperatures between 1200 and 1600 $^\circ C$ for LaB_6. The emission current density for a 2.54cm long insert with inner diameter 6.35mm and net discharge current of 25A is shown, as well as the range if a net return current of +/-10 and 15% are considered. The temperature of the insert for this configuration when a $\dot{m}_{Xe} = 13sccm$ has been measured experimentally [2] and the range is shown as well.

This simplified example shows that the return current and temperature distribution are of great importance. In fact, all of the aforementioned physical details must be considered to develop a more accurate description of LaB_6 hollow cathode operation. We can observe though that the work function for LaB_6 hollow cathodes operated with an internal gas discharge must be lower than the previously reported value of 2.66eV [3] for polycrystalline LaB_6 operating in vacuum. Our previous estimate of the work function for this operating point was ~2.19eV, where assumptions 1,2,3 and 5 were used and the temperature profile along the insert ($T_{insert}(z)$) was extrapolated from three thermocouple measurements and a second degree polynomial fit.

In order to improve the determination of the work function in a LaB_6 hollow cathode that has reached steady state, it is of a paramount importance to accurately determine the net return current (considering space charge limitations), $T_{insert}(z)$, and the impact of the Schottky effect in the work function. If all of those variables were perfectly known, the work function could be determined with higher accuracy than in our previous work. In the present work we have employ

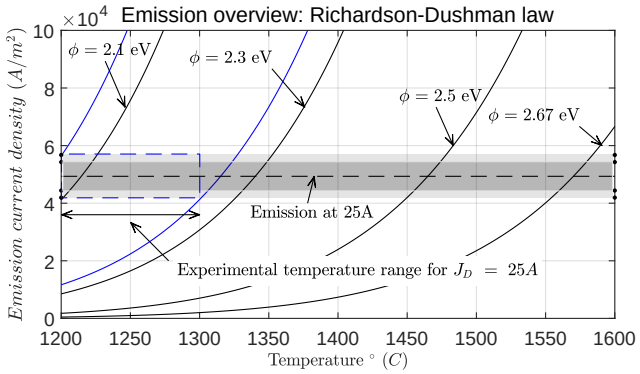

Fig. 1 Thermionic emission sensitivity analysis for Richardson-Dushman law. Uniform emission at $J_D = 25A$ is shown with a +/-10% net return current (dark shaded area) and a +/-15% net return current (lighter shaded area). Experimentally measured temperature range of the insert at $J_D = 25A$ is also shown, as well as the range of work function possible for it.

the JPL in-house plasma solver OrCa2D to find the plasma structure inside the cathode, which provides a quantification of the net return current and Schottky effect.

The question of how to accurately determine the temperature distribution is still challenging to answer. Two experimental approaches have helped establishing the aforementioned temperature in our previous work, i.e. type C thermocouples and sapphire fiber optic-based ratio pyrometry. Even though we continue to improve those techniques with more accurate calibrations, the temperature distribution along the emitting surfaces has uncertainties that impact the proper determination of thermionic emission in a significant manner.

With regards to the thermocouple approach, it is only feasible to measure the temperature at a few locations along the emitting length of the insert, and then the temperature can be interpolated between those points. However, it is difficult to make thermocouple measurements of the temperature at the ends of the insert, which impacts the estimation of the actual shape of $T_{insert}(z)$. Furthermore, type C thermocouples have a 1% inherent tolerance, which gets worse when chained with extension wires, connectors and feedthroughs. The fiber-optic approach also poses challenges in determining $T_{insert}(z)$. Fiber-optics depend on their calibration and a view factor correction method to produce the most accurate temperature profile. When they are used with LaB_6 cathodes, fiber-optics might get coated with La, which could impair their optical properties and shift their calibration. In addition, accurate view factor correction of the unfiltered signal relies on knowledge of the temperature distribution of all the surfaces within view of the insert, data which are not available.

We have developed a third method to improve our understanding of the temperature distribution along the insert and the fidelity of the plasma structure inside hollow cathodes in general, producing a more self-consistent simulation package for hollow cathodes with internal gas discharge. A high fidelity thermal model of the cathode built using the *COMSOL Multiphysics* heat transfer module was experimentally validated and coupled with the in-house OrCa2D plasma solver. An iterative coupling of the two codes is possible due to the slower time scale of the thermal response of the cathode compared to the much faster plasma behavior. Using this coupled OrCa2D-COMSOL solver, we can simulate the temperature distribution that is self-consistently produced at steady state during cathode operation for any geometry, materials used and operating conditions that we establish. Combining the OrCa2D-COMSOL coupled solver with the aforementioned experimental methods brings a significant improvement to the cathode temperature determination problem.

II. Coupled plasma and thermal solution approach

The overall strategy used to couple both codes can be seen in Fig. 2. *MATLAB 2018a* was used as the main framework from which OrCa2D and COMSOL simulation packages are controlled and where the overall decision making takes place. The general process of finding a plasma solution which is consistent with the thermal characteristics of the hollow cathode requires several global simulation/iteration steps.

A global iteration step starts when OrCa2D is provided with a temperature distribution for the insert and the plasma

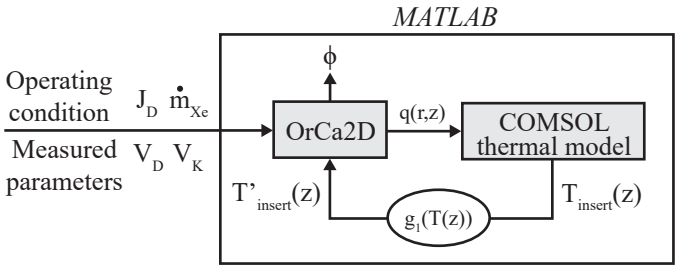

Fig. 2 Overview of the strategy used to compute the coupled solution that includes plasma and thermal models

solution is then obtained for the particular operating point. At that point, OrCa2D produces the heat fluxes to the walls of the cathode from electrons and ions. Those fluxes are then input into the COMSOL heat transfer simulation package where the updated temperature of the insert can be obtained. Then, MATLAB compares the temperature provided to OrCa2D at the beginning of the global iteration step with the temperature profile that COMSOL has generated using the plasma heat fluxes. If they are not the same, the accommodating function $g_1(T(z))$ shown in Fig. 2, Eq. 2 creates a new temperature profile to input into OrCa2D, which is closer to the one that COMSOL computed in the previous global iteration step. In order to input $T'_{insert}(z)$ into OrCa2D, a forth order degree polynomial fit is used. Then, a new global iteration can be computed. The code finishes when the temperature input into OrCa2D and the one computed by COMSOL heat transfer module differ by a small tolerance. The root mean square error (RMSE) of both profiles is computed and convergence is defined when this value is less than 10. At that point, we conclude that the plasma solution is self-consistent with the thermal model of the cathode.

$$T'(z)_{i+1} = \begin{cases} T(z)_i & if \;\; |T(z)_i - T'(z)_i| < dT_{cap} \;\; \forall z \\ T'(z)_i + (T(z)_i - T'(z)_i)/F & if \;\; |T(z)_i - T'(z)_i| >= dT_{cap} \;\; \forall z \\ where \;\; T = T_{insert}, \;\; dT_{cap} = parameter & , \;\; F = max(|T(z)_i - T'(z)_i|)/dT_{cap} \end{cases} \tag{2}$$

With this self-consistent solution we are able to capture the details of the shape of $T_{insert}(z)$, along with a high fidelity estimate of the net return current and Schottky effect. We did not include in the present work the influence of the work function variations along the insert, nevertheless, the coupled platform can account for it in a straightforward way.

A. Hollow cathode thermal model

The thermal model used in this study was created using *COMSOL Multiphysics* V5.3a. The geometry was built using SOLIDWORKS 3D CAD 2016 and imported into COMSOL. Two "Physics" modules were used to model heat transfer by conduction and radiation between components, "Heat Transfer with Surface-to-Surface Radiation" and "Heat Transfer in Thin Shells". The meshing approach was based on a parameterization using a combination of maximum sized elements in the edges of the domains and "extremely fine refinement" for the interior of the domain. The thermal model was written in batch mode in Java which allows the main strategy that controls the coupled Plasma-Thermal model (Matlab) to execute per request, enabling dynamic creation of thermal models. An example of the solution of such strategy is shown in Fig. 3

1. Geometry and materials

The geometry of the cathode thermal model is a 2D axisymmetric approximation of the actual cathode geometry. The different parts and materials used are shown in Fig. 5 and Table 1. The mounting plate (Part 7) is a fictitious boundary at which a fixed temperature equal to that measured at a corresponding point on the cathode tube is specified. In reality the cathode is attached to an aluminum block 0.5" further upstream.

The heater coil is manufactured with an inner diameter slightly smaller than the cathode tube outer diameter so it presses against the tube when installed around it. Because the heater and cathode tube are both mode of pure Ta and are pressed together, during operation at high temperature they eventually fuse to each other. This interaction between the two parts was modelled with a point contact between the individual heater coils and the cathode tube. Thermal conductivity and total hemispherical emissivity values for the different materials used in the cathode construction were

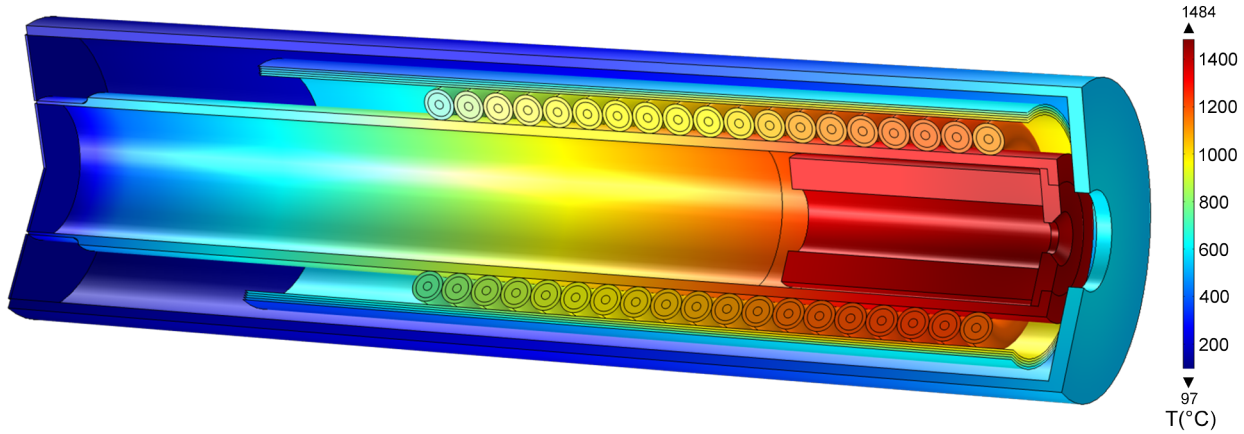

Fig. 3 Temperature distribution created with COMSOL (example).

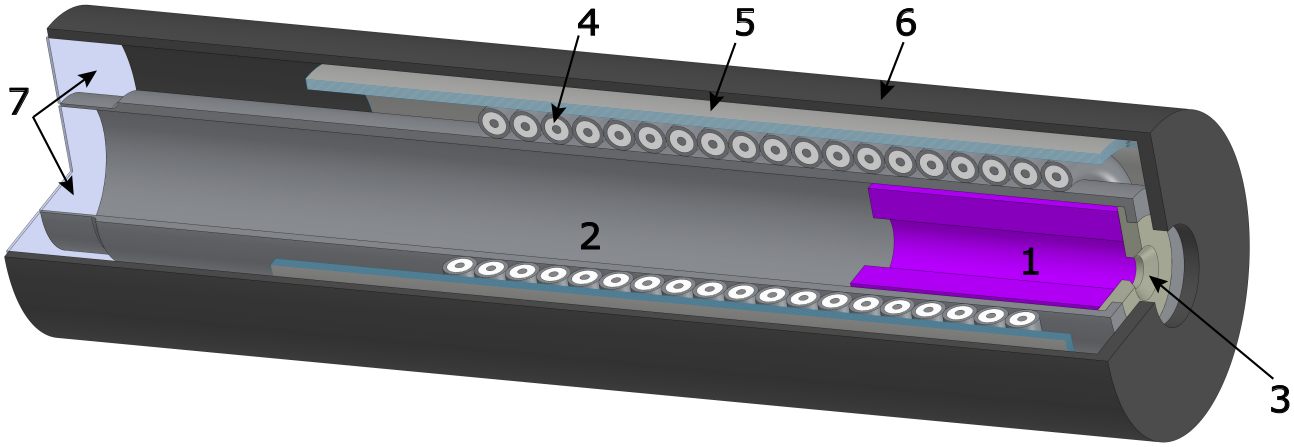

Fig. 5 Cathode geometry.

obtained from the literature and the references are shown in Table 1. Tantalum total hemispherical emissivity is shown in Fig. 4.

2. Thermal modelling

In the present work the thermal model of the cathode assumes axisymmetry (2D model), as shown in Fig. 6. The only component that is not axisymmetric in reality is the heater, which is made from a long cable, thus, there is heat conduction along the heater length. In the model the heater is made of 19 tori arranged along the axis of symmetry of the cathode, starting from the one that is most downstream. They were modelled with point contacts in the same way as the heater-cathode tube interface, therefore, heat can flow between coils. The heater consists of 3 components, the inner wire, insulator and outer sheath. It was assumed that those three components are in perfect thermal contact, as they are manufactured with a swagging process.

Cathode geometry and materials			
Part number in Fig. 5	Name	Material	Material properties
1	Insert	LaB_6	[5], [6]
2	Cathode tube	Ta	[7], [4]
3	Orifice plate	W	[7], [8–10]
4	Heater	Ta *and* Al_2O_3	[7], [4], [11]
5	Radiation shielding	Ta	[7], [4]
6	Keeper	C	[12], [13]
7	Mounting plate	Al 6061	[14], [15]

Table 1 Summary: cathode parts and materials

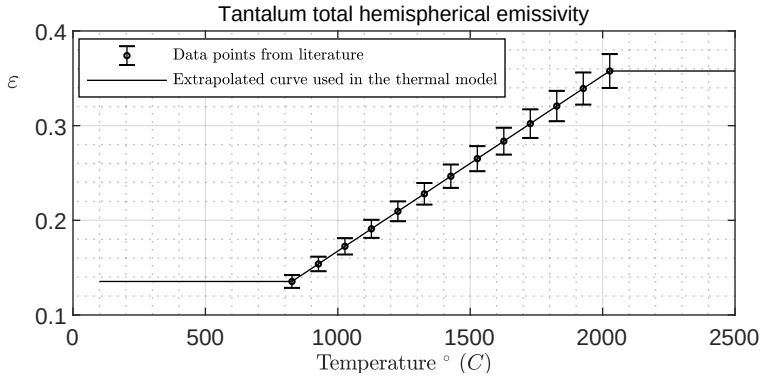

Fig. 4 Ta total hemispherical emissivity from [4]

The insert is assumed to be non-porous and in perfect thermal contact with the orifice plate. The orifice plate was modelled as having perfect thermal contact with the cathode tube. The radiation shielding was modelled with 5 layers instead of 10 as it is in reality. This reduction in the number of shields is a way to approximate the thermal contact between layers, which we found was necessary to match measure temperatures. Each radiation shield was modelled using "Heat Transfer in Thin Shells" where the governing equations associated with the thermally thin approximation are implemented (no temperature gradient across the layers). The radiation shielding used was 0.001" thick. Additionally, the radiation shields were observed to have darkened during cathode operation by an unknown source. An additional 0.2 was added to the literature value for the emissivity curve of Ta on these layers, this configuration is named the *baseline* thermal model. The sensitivity to this parameter was studied with a second model which assumed the emissivity was higher by 0.4 (i.e., one time the increase above values used in the *baseline* case). The graphite keeper emissivity was assumed to be unity.

All the components were modelled from the radiation standpoint as diffuse gray surfaces (no wavelength dependence of emissivity). The hemicube approximation was used to compute the form factors taking into account shadowing effects. A value of 256 (COMSOL default) was used for the radiation resolution, a parameter which controls the accuracy of the method [16–18]. We are using axisymmetric geometry, therefore, the 2D geometry needs to be virtually revolved to create a 3D one where values for the mutual irradiance and view factors can be computed. 128 azimuthal sectors (COMSOL default) were used for this process. The thermal solution sensitivity was studied against grid refinement, radiation resolution and azimuthal sectors. The outcome of that analysis showed that the temperature

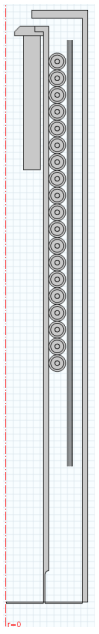

Fig. 6 Axisymmetric model of the hollow cathode.

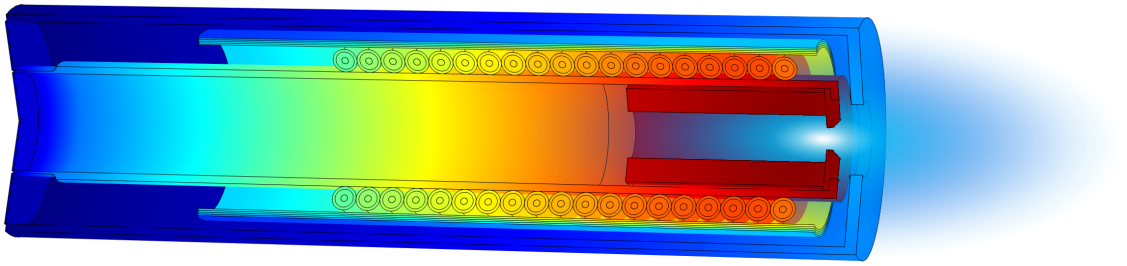

(a) Thermal model and plasma model (artistic representation) results.

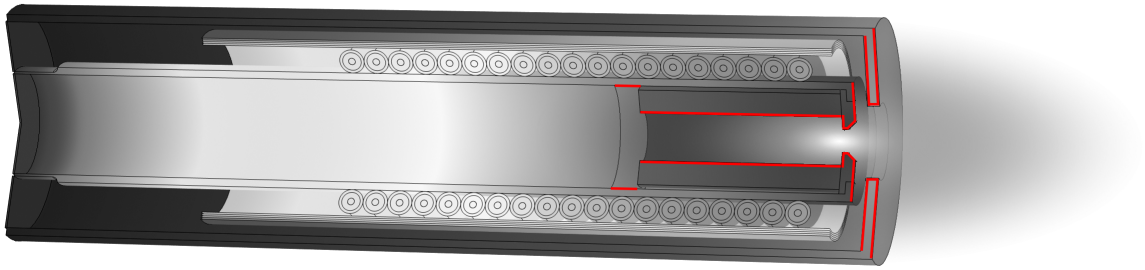

(b) Surfaces where the plasma heat fluxes are input into the thermal model geometry (highlighted in red)

Fig. 7 Representation of the cathode thermal model, plasma and surfaces at the interface.

distribution does not change significantly (only 1 to 2 degrees) with increasing the radiation resolution and the number of azimuthal sectors.

3. Thermal fluxes - the interface with the plasma solver

Heat from the plasma is input into the model as heat fluxes along the surfaces shared by both codes. These surfaces are highlighted in red in Fig. 7. The approach followed for this interaction is based on extracting the heat fluxes from the plasma at every grid point of the plasma boundary and interpolating their value at every grid point of the thermal model boundary. The total heat input into any surface was used to check the success of the approach.

B. Plasma model

All plasma simulations presented herein have been performed with the 2-D axisymmetric solver of the partially ionized gas in hollow cathode discharges called OrCa2D. Development of the code began in 2004 and since then it has been used to simulate numerous hollow cathodes, operating under a wide range of conditions [19–25]. Comparisons with several plasma measurements (e.g. [25, 26]) have helped improve both our understanding of driving processes inside these devices as well as the fidelity of the code.

The physics models, conservation equations and numerical methods in OrCa2D have been described in detail in previous articles [19, 20, 22, 24] and will only be described briefly here. The code solves the conservation laws for three species in the partially-ionized gas: electrons, xenon ions and xenon neutrals. It is assumed that only singly-charged ions are present and that quasi-neutrality prevails except inside sheaths which are handled with appropriate boundary conditions. The Navier-Stokes equations are solved for the neutral gas only inside the cathode up to a "transition boundary" at which the method to obtain the solution changes to a collision-less approach that assumes neutrals follow straight-line trajectories [27]. The Euler equations for mass and momentum of ions are solved in the entire computational domain. A separate energy equation also is solved for the ions allowing for distinct temperatures between the two heavy species. Ionization, charge exchange and electron-ion collisions are accounted for in the equations and modeled as source or drag terms. The solution for the electrons is obtained from a combination of Ohm's law, energy and current

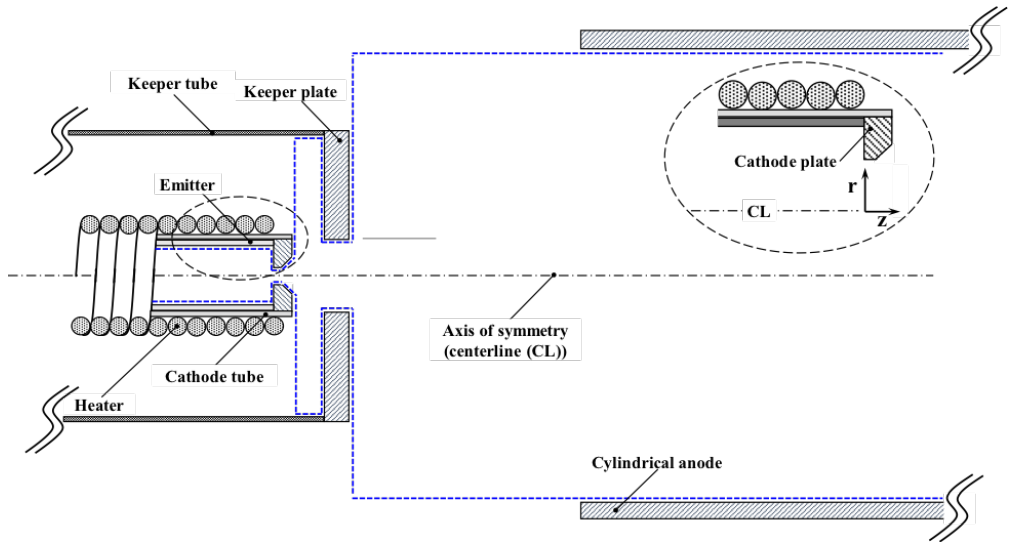

Fig. 8 Schematic of the computational domain (blue dashed outline) used in the OrCa2D simulations, in a region near the cathode electrodes and plume (not to-scale).

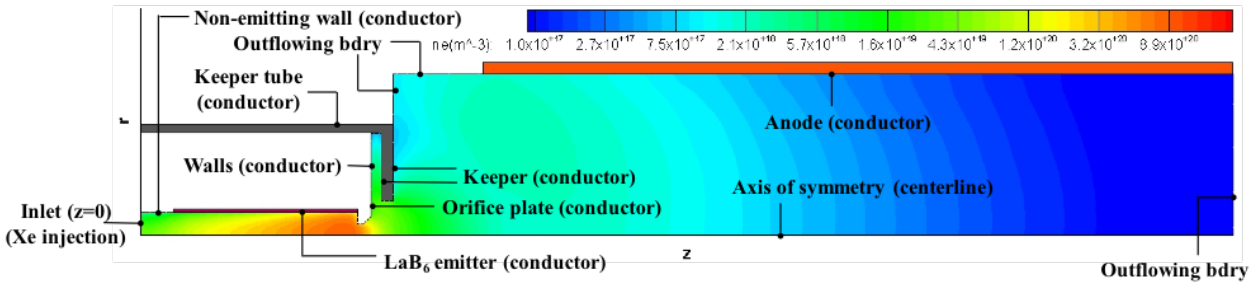

Fig. 9 OrCa2D numerical simulation (half) domain showing naming conventions for all relevant boundaries of the LaB6 cathode. (Also shown is the simulation result for the electron number density, n_e (the details of which are described later in this article).

conservation equations. An idealized model for the anomalous enhancement in the resistivity, which is now known to occur in the cathode plume [28, 29] due the excitement of ion acoustic turbulence (IAT) there, is included in Ohm's law. The model is based on the formulations of Sagdeev and Galeev (S&G) [30] and is described in more detail in our companion paper by Mikellides, et al., [31].

The emitted electron current density from the insert is specified according to the Richardson-Dushman equation for thermionic emission [32]. The emitter temperature is implemented as a boundary condition in OrCa2D using a 4th-order (or lower) polynomial that provides the temperature as a function of axial position along the emitter. The field-enhanced emission due to the Schottky effect is included as derived in [20], and its implementation in OrCa2D is described in [33]. The work function must be provided and its value is assumed presently to remain fixed along the entire emitter. It is important to emphasize that net emission is determined not only by the emission current density but also by the current density of electrons and ions that are absorbed by the emitter wall. This is also accounted for in OrCa2D as described in [19, 20]. For boundaries that are electrically conducting, electron and ion collection is accounted for in both limits of ion-attracting and an ion-repelling sheaths. This boundary condition was described in detail in [23]. At the anode, current is collected as specified by the discharge current. At the anode, it is also assumed that ions become neutralized after they strike it and return back to the computational region as neutrals with a thermal speed that is based on the specified temperature of the anode.

In the experiments that provided the conditions and measurements for the cathode investigated here, a cylindrical anode was used [2]. The OrCa2D computational domain in the vicinity of the cathode plate and near plume is outlined in Fig. 8. The full domain from a representative simulation of the cathode is shown in Fig. 9. The two figures also provide naming conventions for the various cathode components and boundary conditions that are relevant to this study. The inlet boundary is defined to be at z=0 in the domain. The keeper was set to collect no net current (i.e. it was floating), which was accounted for in the simulations through appropriate boundary conditions. A zero-current condition also was specified at the out-flowing boundaries (Fig. 9). A magnetic field was not applied in the experiments or the simulations.

The highest Xe^+ number density expected in the cathode is on the order of $n_{i\_max} = 10^{21}\ m^{-3}$. Using that estimate for the plasma density, the photon mean free path based on the Planck opacity or the Rosseland opacity is much larger than 10cm and 2.5m respectively [34, 35]. Thus, the plasma is considered transparent and it does not interact with the thermal radiation mechanisms described above.

At every global iteration step, a new temperature profile is input to the plasma solver. OrCa2D was configured to find the plasma solution that provides the keeper voltage that matches the experimentally measured value of V_K. Then, the new heat fluxes associated with the converged plasma solution are input into the thermal model in order to generate an updated temperature profile for the insert ($T_{insert}(z)$). This is one of the many approaches that can be used to update the plasma solution at every iteration. This approach provided the most stable convergence in the global sense because the plasma solution is always close to the one that matches the experimental value of V_K, and only the heat fluxes are being influenced by the small changes in the plasma distribution and the updated value of the work function.

During the simulation, the evolution of the plasma solution is monitored by several numerical probes positioned throughout the computational domain. A convergence criterion has been implemented in OrCa2D that is based on the time-averaged computed variables. The algorithm computes the percent change in the main plasma variables within a specified time increment, from all numerical probes. The simulation is terminated when the maximum percent change is less than a specified value. The Matlab framework was built to be able to manipulate this convergence criterion as needed. The current configuration requires the plasma solver to produce more accurate results as the global simulation gets closer to the self-consistent solution. This strategy optimizes global convergence computational time without affecting the fidelity of the final solution.

III. Thermal model validation

An experimental validation process was used to determine the fidelity of the COMSOL thermal model. Using the cathode heater, five power levels (P = 124.53, 157.19, 192.62, 229.9, 267.78 W corresponding to experiments 1,2,3,4 and 5 in Fig. 11 & 12) were applied to the cathode. Seven thermocouples were used to measure the temperature in the positions shown in Fig. 10. Two of those thermocouples (TC6 and TC10) were used as boundary conditions for the validation process, the other 5 were used to compare experimental with simulated thermal results.

The heater was powered with a DC power supply. The current was measured with a shunt placed along the heater circuit which provides 10mA accuracy. The voltage of the heater was measured at the vacuum feedthrough. There is approximately 2 m of cable connecting the feedthrough to the heater. The resistance of that cable was measured and used to correct for the voltage drop along the cables when the heater is powered. The voltage measurement has an

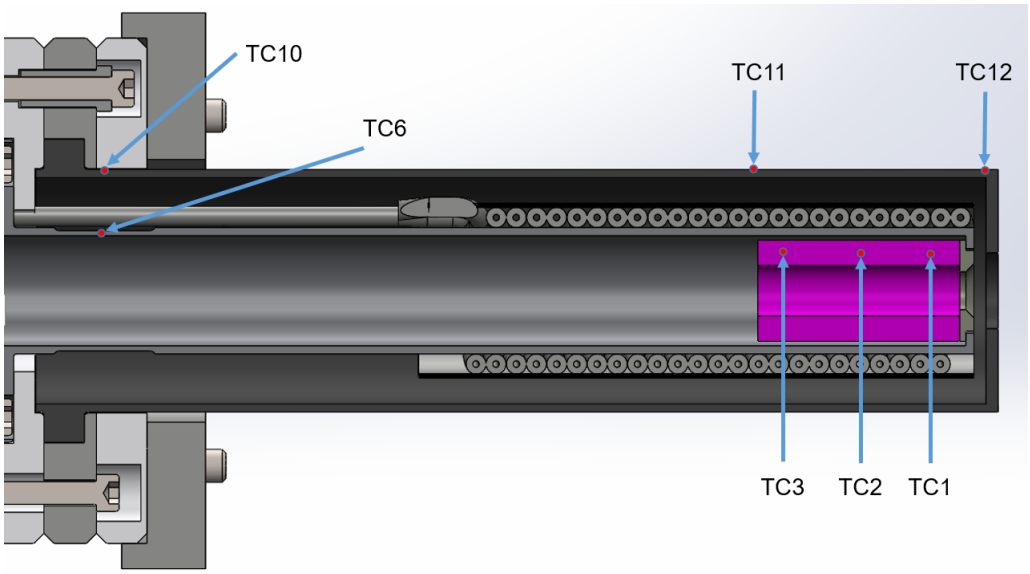

Fig. 10 Location where the thermocouples were installed

accuracy of 50mV. A Keithley 2400-C sourcemeter was used to calibrate the data acquisition system. In the thermal model, the distribution of power over the heater was modeled by calculating the Joule heating produced in the inner conductor of each coil using the temperature-dependent electrical resistivity [36] for a given current. The current was varied until the sum of the power dissipated in the coils matched the experimental value. Thus, the current necessary to match the measured total power is self-consistently obtained during the thermal model simulation and a more realistic distribution of power is simulated.

There is a section of the heater (see Fig. 10) that is not included in the thermal model but consumes part of the heater input power. The power associated with that part of the heater was estimated using a linear variation of the temperature along the heater lead and electrical resistivity from [36]. This calculation yielded 5% as the maximum percentage of the power associated with the part of the heater not modelled. In order to take into account the effect of this portion of the power input, five more thermal simulations where performed with power reduced by 5% from the measured power. With those extra five temperature distributions we can bound the effect of not including that portion of the heater in the model.

The results of the described thermal model validation process can be observed in Fig. 11. There are 10 plots in total. The five plots on the top show absolute temperature for TC1, TC2, TC3, TC11, TC12 for the five power levels. The experimental results are shown in blue (temperature measured with thermocouples in the cathode). The COMSOL thermal model results are shown in red. The results of the COMSOL thermal model when 95% of the heater power is input instead of the experimentally used power levels are shown in green. The five plots on the bottom show the differences between simulated and experimental results. Bar plots show the rated thermocouple accuracies.

Assuming the thermocouples measured the correct temperature value, the COMSOL thermal model results for TC1, TC2 and TC3 produce a maximum of 60 $^{\circ}C$ absolute error. This error is reduced to a maximum of 31 $^{\circ}C$ for TC11 and TC12.

We have described and validated the *baseline* thermal model used in the coupled simulation package. In addition to that thermal model, a slightly different one was created and used in a sensitivity analysis that we will introduce later in this paper. This new thermal model underestimates the global thermal losses of the cathode, and therefore, for any given power input, the temperature distribution of the inner region (insert region) is colder than the experimental values, see Fig. 12. The only difference between this thermal model and the *baseline* is that we have added 0.4 to the ε_{Ta} from literature in the material properties utilized to model the radiation shield, as opposed to 0.2 used in the *baseline*.

In Fig. 12 we have simplified the validation results by removing the absolute values of the experiments and simulations that we showed in Fig. 11. As TC1, TC2 and TC3 give very similar results due to their physical proximity, we only show results for TC2. We have also removed the two simulation series (P = 100% and P = 95%), and only show the mean temperature simulated by both. Results for this thermal model show that TC2 is cooler than the experimental results by a minimum of ~30 $^{\circ}$ (C) and a maximum of ~110 $^{\circ}$ (C). In addition, the new thermal model estimates ~70

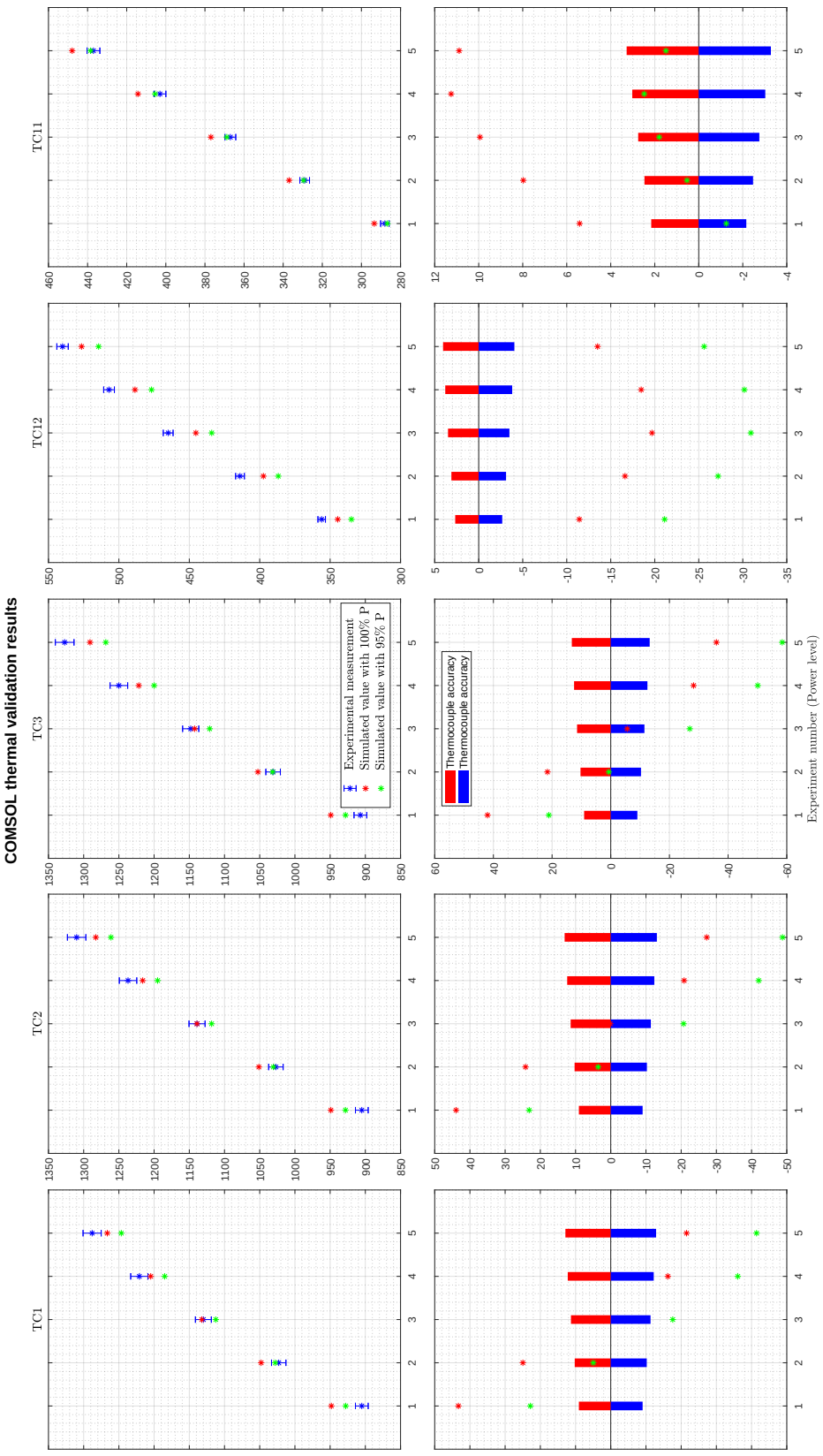

Fig. 11 COMSOL thermal model validation results

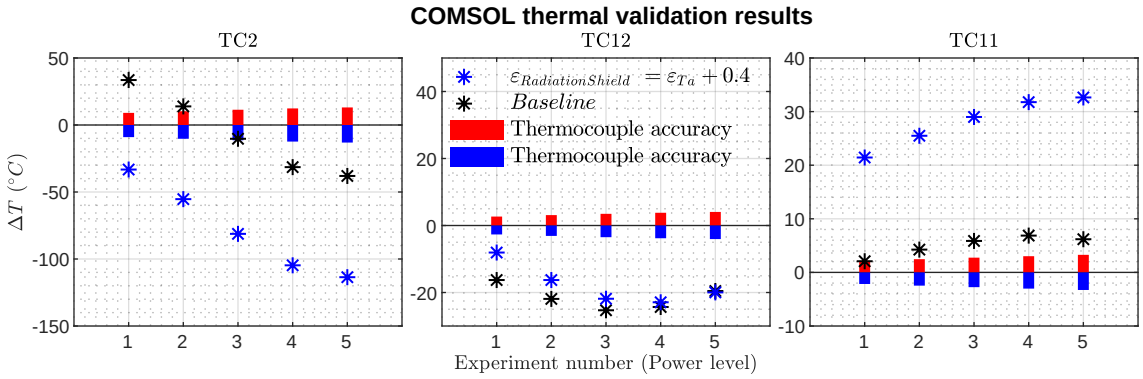

Fig. 12 COMSOL thermal model validation results. Comparison between thermal model *baseline* and modified version with 0.4 addition to the emissivity of the radiation shield.

° (C) cooler temperatures for all power levels than the *baseline*. This thermal model will be useful to bound the effect of the *baseline* thermal behavior in the coupled plasma-thermal simulation.

IV. Results and discussion

We employed the novel scheme described above to study the self-consistent solution of a LaB_6 cathode running at J_D=25 A and $\dot{m}_{Xe}$=13 sccm. The keeper and discharge voltage used were the experimentally measured values of $V_K = 4.2V$ and $V_D = 25V$.

A. Results

1. Initial plasma solution for the coupled plasma-thermal simulations

To start the coupled plasma-thermal simulations an initial solution of the plasma must be provided. This is obtained with OrCa2D as follows. The mass flow rate and discharge current are required as inputs to the simulation. They are therefore specified directly in the code based on the conditions under which the experiment was conducted, namely 13 sccm and 25 A. To achieve the specified discharge current, an iteration is performed on a single coefficient that determines the level of resistivity enhancement due to the IAT in the cathode plume, as described in more detail in our companion paper by Mikellides, et al. [37]. The discharge voltage is set in the simulations at 25 V to match the experiments. The temperature along the emitter $T_{insert}(T)$ is specified using a second degree polynomial fit to measurements obtained by Guerrero, et al., [2] using three type C thermocouples, see Fig. 14. The simulation iterates on the value of the work function that yields the measured keeper voltage of 4.2 V.

In the simulations presented here, the convergence criterion was set to 0.002%. The steady-state solution for the plasma potential (ϕ), electron temperature (T_e) and neutral number density (n_n) is provided in Fig. 13. The electron number density (n_e) was shown earlier in Fig. 9. The steady state value of the work function was found to be 2.2293 eV, slightly higher than ~2.19 eV previously estimated [2]. This new value is a more accurate prediction (~0.04eV higher) because we have taken into account the net return of electrons and ions to the insert and the Schottky effect. The net return is ~4.5 A to the insert and ~0.5 A to the other cathode surfaces, requiring a net thermionic emission of ~20 A. This means that the net return current is ~20% of the discharge current for this operating condition. This effect, coupled with the reduction of ϕ due to the Schottky effect, explains the increase in the estimated work function. We can improve this estimate further when we consider the temperature profile that comes from the COMSOL thermal model. We will eventually include the variation of the work function along the insert as well.

As noted earlier, the plasma solution in Fig. 13 is used to calculate the initial heat fluxes for the coupled plasma-thermal simulations. During the coupled simulations the approach to obtain the steady-state OrCa2D solution at each intermediate global iteration remains essentially the same. The exception is that at each iteration a new polynomial fit to the emitter temperature is defined at the OrCa2D emitter boundary, based on the solution provided by the thermal model. With the newly defined temperature, OrCa2D then proceeds to obtain the new steady-state solution by performing the two aforementioned iterations in parallel, namely on the anomalous transport coefficient to attain the specified discharge

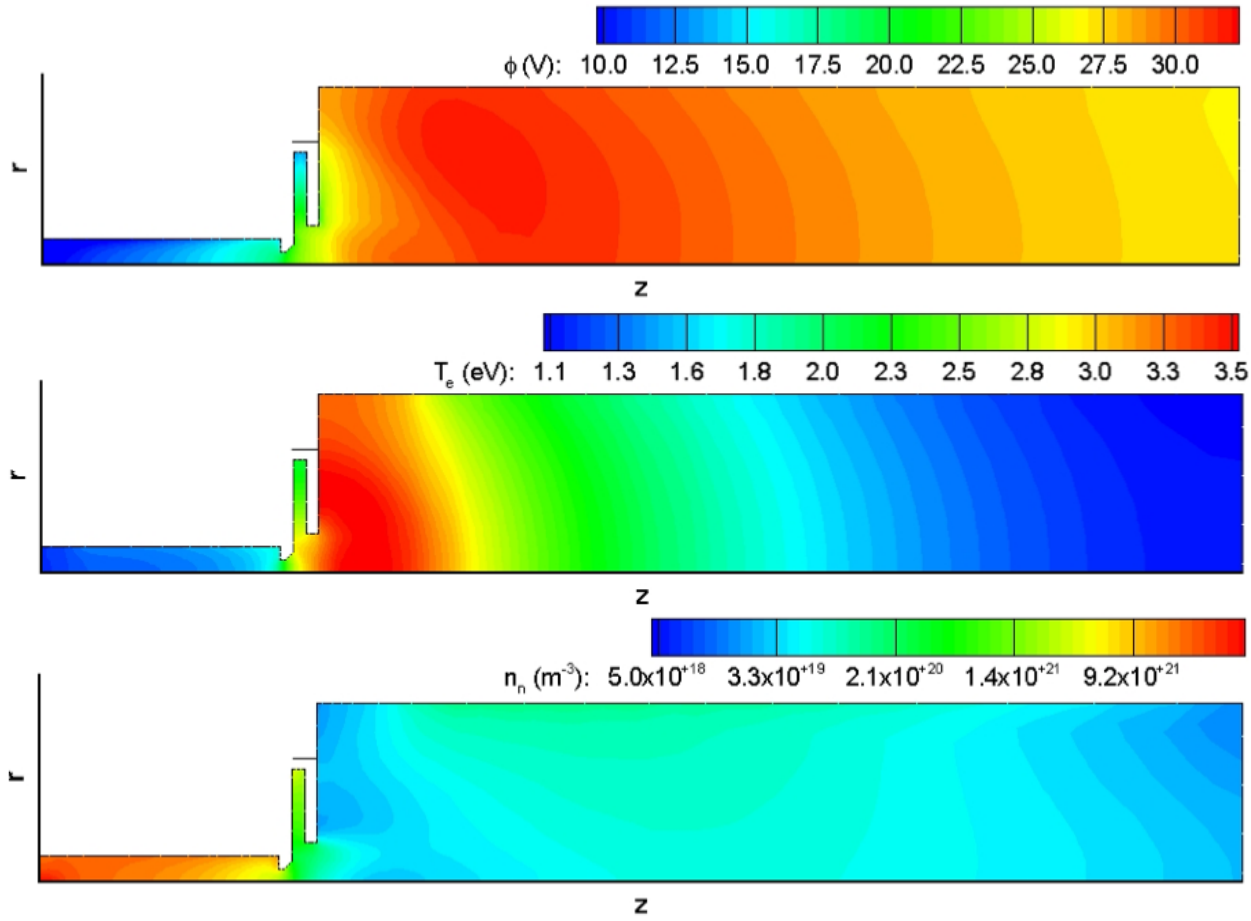

Fig. 13 Steady-state solution for the plasma potential (ϕ), electron temperature (T_e) and neutral gas density (n_n) from the OrCa2D simulations with the initial emitter temperature profile shown in Fig. 14 The solution was used to calculate the initial heat fluxes for the coupled plasma-thermal simulations.

current (25 A) and on the work function to attain the measured keeper voltage (4.2 V).

2. Converged coupled solution

Initializing the coupled plasma-thermal model with the aforementioned plasma solution produces the evolution of temperature $T_{insert}(z)_i$ and $T'_{insert}(z)_i$ at every global iteration step i, as shown in Fig. 15. The self-consistent solution ($T_{insert}(z)_i = T'_{insert}(z)_i$) is shown in blue in Fig. 14.

3. Comparison to measured temperatures - sensitivity analysis

In order to estimate the sensitivity of this coupled system we varied 3 parameters and ran the global simulation until the converged solutions of the system were found. These included keeper voltage ($V_K = 3.5V$), ε_{Ta} (20% increase with respect to the literature values), $\varepsilon(T)$ used in the definition of the radiation shield (0.2 increase above the value used in the *baseline*). Results are shown in Fig. 14

B. Discussion

The converged solution is defined by the COMSOL thermal *baseline* model and the OrCa2D plasma solution necessary to match V_D & V_K at the operating point utilized in this simulation. Coupling both models imposes an additional constraint in the solution, therefore, one less degree of freedom is available. Thus, ϕ and $T_{insert}(z)$ are the inherent results of this coupled system.

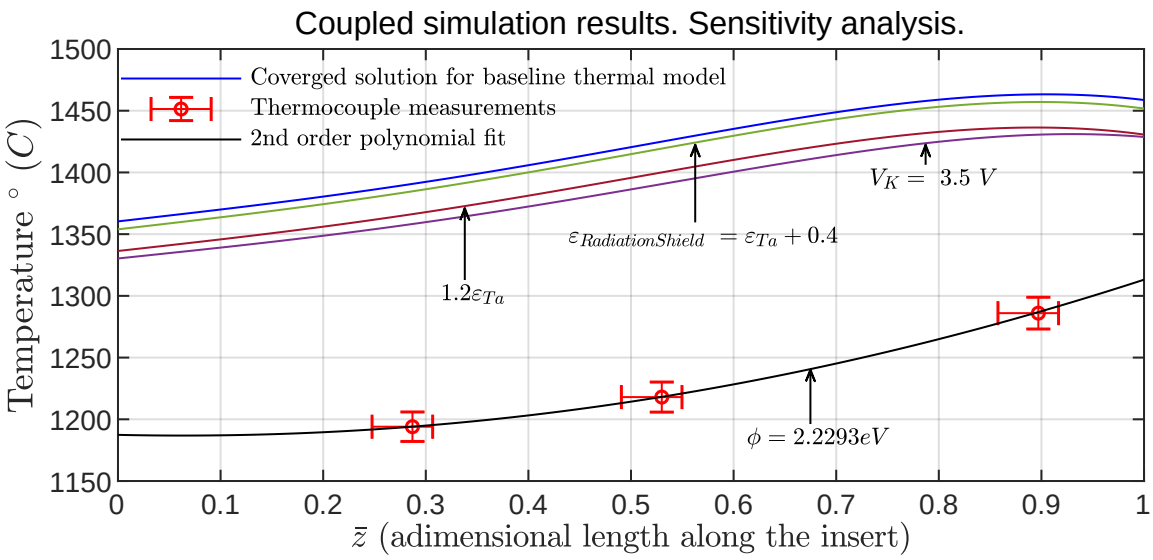

Fig. 14 Converged temperature results for the *baseline* thermal model and sensitivity analysis. Also shown: experimental measurements and 2nd order polynomial fit.

We have shown in Fig. 15 that the simulation approach is successful and convergence occurs. Notably, the converged insert temperature profile does not match the thermocouple measurements, with the solution predicting higher temperature than that estimated by thermocouple measurements. The thermocouple measurement approach was thoroughly analyzed in our previous work [2], and we concluded that the discrepancy observed in the coupled converged solution cannot be explained by an inaccuracy of the temperature measurements. Possible explanations of the observed discrepancy between the predicted and measured temperature values are discussed below.

1. Thermal modelling accuracy: underestimation of losses

One possibility to explain why the predicted temperature is higher than the measurements is associated with inaccuracies in the thermal model definition. To understand the sensitivity of the thermal model to the different parameters that define it, we studied the impact of parameter variations from the *baseline* (data not shown). The most sensitive parameter in the cathode thermal behaviour is ε_{Ta} used to model the cathode tube, the heater and the radiation shield. The emissivity of Ta (ε_{Ta}) in the literature is obtained for pure polished material. We observed darkening of different Ta cathode components, indicating impurities, that may increase the actual ε_{Ta}. The darkening was particularly prominent on the radiation shielding, therefore, we used a value of ε_{Ta}+0.2 for this component in order to obtain the agreement shown in Fig. 11.

When we increase the value of the emissivity for modelling the radiation shield by 0.4 above the literature values, we are effectively overestimating the losses in the cathode as shown in Fig. 12 by the cooler response of the insert. However, that does not affect the response of the coupled solution significantly (Fig.14)

A more significant overestimation of the losses was performed by using 120% of the literature values for the Ta emissivity. The response in the converged solution using this modified thermal model was still not significantly cooler. Therefore, the discrepancy between the global simulation and the experimental values cannot be explained by any reasonable increase in the heat losses.

The *baseline* thermal model will be improved by experimentally testing individual components or small sub-groups of components of the cathode and comparing the results with corresponding thermal simulations. In that manner we can likely reduce the variability observed in Fig. 11 over the different power settings. Those studies would focus on trying to measure a more realistic emissivity for Ta in the actual components using a calibrated thermal camera. In addition, an improved modelling technique will be used to simulate the radiation shield and the contact between cathode tube and heater coils. However, given the results of the sensitivity analysis for the overestimation of the global heat losses of the cathode, it is unlikely that refining the thermal characteristics of the cathode will explain the difference between temperature measurements and the self-consistent solution.

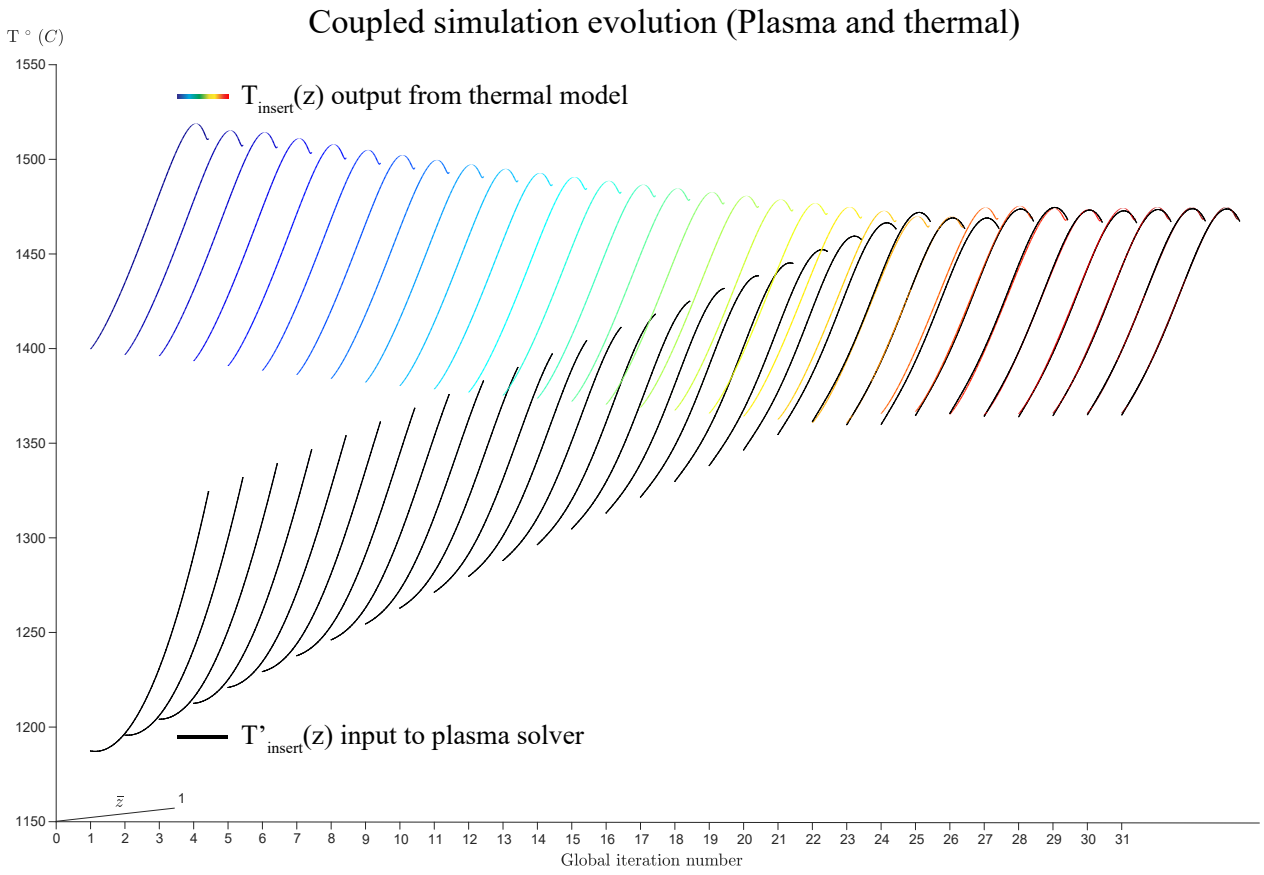

Fig. 15 Evolution of the temperature input to OrCa2D (black curves) and output from COMSOL thermal model based on heat fluxes from the last iteration of OrCa2D (colored curves)

2. Plasma modelling sensitivity

The discrepancy between the predicted and observed temperature values could also be related to inaccuracies in the plasma solver. The plasma solution depends on four experimentally measured variables and the modelling techniques.

We found that the four empirical variables - $\dot{m}_{Xe}$, J_D, V_D, and V_K - were measured with accuracies that do not affect the final solution significantly. However, the modelling of V_K inside the plasma code strongly depends on the fidelity of the molecular flow solution around the keeper and the extent of the plasma domain. We studied the sensitivity to V_K by reducing it to 3.5V. The self-consistent insert temperature solution was reduced by ~40 $^\circ C$ in this case. This result suggests that inaccuracies in V_K modelling are not a likely explanation of the observed difference between experimental and modelling results.

It is of major interest to measure the distribution of internal plasma parameters and compare them to the converged solution to check whether the plasma solution models well the real plasma structure. The heat fluxes are dominated by the the ion return current contribution. Partial energy accommodation of ions bombarding the walls [38] is another potential contributor to the discrepancy we observed.

The work function used in this coupled system was a constant. However, there is experimental evidence that suggests that the work function is not a constant along the insert of the cathode during operation [2]. In the future we will study solutions based on a parameterized $\phi(z)$. In this case, more information from the plasma is necessary, otherwise the system is not well defined and therefore a unique solution cannot be found among the several numerically possible.

Acknowledgments

We thank Ray Swindlehurst and Nowell Niblett for technical support, Alejandro Lopez Ortega for help with the plasma solver. Portions of the research described in this paper were carried out at the Jet Propulsion Laboratory,

California Institute of Technology, under a contract with the National Aeronautics and Space Administration.

References

[1] Walter H. Kohl, *Handbook of materials and techniques for vacuum devices*, AIP-Press, 1997.

[2] Guerrero, P., Polk, J. E., Richter, M. H., and Lopez Ortega, A. L., "Work function reduction in lanthanum hexaboride hollow cathodes operated in gas discharges," *35th International Electric Propulsion Conference*, 2017, pp. 2017–399. URL https://iepc2017.org/sites/default/files/speaker-papers/iepc-2017_399.pdf.

[3] Lafferty, J., "Boride Cathodes," *Journal of applied physics*, Vol. 22, No. 3, 1951.

[4] Milošević, N. D., Vuković, G. S., Pavičić, D. Z., and Maglić, K. D., "Thermal Properties of Tantalum Between 300 and 2300K," *International Journal of Thermophysics*, Vol. 20, No. 4, 1999, pp. 1129–1136. doi:10.1023/A:1022659005050, URL http://link.springer.com/10.1023/A:1022659005050.

[5] Tanaka, T., "The thermal and electrical conductivities of LaB6 at high temperatures," *Journal of Physics C: Solid state physics*, Vol. 7, 1974, pp. 177–180.

[6] Storms, E. K., "The emissivity of LaB6 at 650 nm," *Journal of applied physics*, Vol. 4450, 1979. doi:10.1063/1.326438.

[7] Ho, C. Y., Powell, R. W., and Liley, P. E., "Thermal Conductivity of the Elements: A comprehensive review," , 1974. doi:10.1063/1.3253100.

[8] Company, G. E., and Park, N., "Radiating Characteristics of Tungsten and Tungsten Lamps," *Journal of the Optical Society of*, Vol. 35, No. 2, 1945, pp. 108–113. doi:10.1364/JOSA.35.000108.

[9] Worthing, A. G., and Forsythe, W., "Total emissivity powers and resistivities of tungsten at incandescence," *Physical Review*, Vol. 18, 1921, pp. 144–147.

[10] Forsythe, W., and Watson, E., "Resistance and radiation of tungsten as a function of temperature," *Josa*, Vol. 249, No. 1925, 1934, pp. 114–118. URL http://www.opticsinfobase.org/abstract.cfm?id=48776.

[11] Kingery, W., Francl, J., Coble, R., and Vasilos, T., "Thermal conductivity: X, Data for Several Pure Oxide Materials Corrected to Zero Porosity," *Journal of the American Ceramic Society*, Vol. 37, No. 2, 1953, pp. 107–110.

[12] Weisenburger, S., "Heat transport measurements in polycrystalline graphites up to 2600C (Report on an international cooperative measuring programme)," *High Temperatures - High Pressures*, Vol. 5, 1973, pp. 475–480.

[13] Zhang, B., Redgrove, J., and Clark, J., "New apparatus for measurement of the spectral, angular, and total emissivity of solids," *High Temperatures - High Pressures*, Vol. 35-36, No. 3, 2003, pp. 289–302. doi:10.1068/htjr124.

[14] N/A, *Military Handbook - MIL-HDBK-5H: Metallic Materials and Elements for Aerospace Vehicle Structures*, U.S. Department of Defense, 1998.

[15] Wen, C.-d., and Mudawar, I., "Experimental Investigation of Emissivity of Aluminum Alloys and Temperature Determination Using," *Journal of Materials Engineering and Performance*, Vol. 11, No. October, 2002, pp. 551–562.

[16] Cohen, M., and Greenberg, D., "The hemi-cube: A radiosity solution for complex environments," *ACM SIGGRAPH Computer Graphics*, Vol. 19, No. 3, 1985, pp. 31–40. doi:http://doi.acm.org/10.1145/325165.325171, URL http://dl.acm.org/citation.cfm?id=325171.

[17] Meyer, U., "Hemi-Cube Ray-Tracing : A Method for Generating Soft Shadows," *Eurographics 90*, 1990, pp. 365–376.

[18] Emery, a. F., Cochran, R. J., Dillon, H., and Mescher, a., "Validation of Radiation Computations using Viewfactors and COMSOL ' s Hemicube Approaches," *COMSOL Conference 2009 Boston*, 2009.

[19] Mikellides, I. G., and Katz, I., "Wear Mechanisms in Electron Sources for Ion Propulsion , 1 : Neutralizer Hollow Cathode," *Journal of Propulsion and Power*, Vol. 24, No. 4, 2008. doi:10.2514/1.33461.

[20] Mikellides, I. G., Katz, I., Goebel, D. M., and Polk, J. E., "Hollow cathode theory and experiment. II . A two-dimensional theoretical model of the emitter region," *JOURNAL OF APPLIED PHYSICS*, 2005, pp. 1–14. doi:10.1063/1.2135409.

[21] Mikellides, I. G., Katz, I., Goebel, D. M., Polk, J. E., and Jameson, K. K., "Plasma processes inside dispenser hollow cathodes," *Physics of Plasmas*, Vol. 13, No. May, 2006, p. 063504. doi:10.1063/1.2208292.

[22] Mikellides, I. G., Katz, I., Goebel, D. M., Jameson, K. K., and Polk, J. E., "Wear Mechanisms in Electron Sources for Ion Propulsion , 2 : Discharge Hollow Cathode," *Journal of Propulsion and Power*, Vol. 24, No. 4, 2008. doi:10.2514/1.33462.

[23] Mikellides, I. G., Goebel, D. M., Snyder, J. S., Katz, I., and Herman, D. A., "The discharge plasma in ion engine neutralizers : Numerical simulations and comparisons with laboratory data," *Journal of Applied Physics*, 2010, pp. 1–12. doi:10.1063/1.3514560.

[24] Mikellides, I. G., "Effects of viscosity in a partially ionized channel flow with thermionic emission," *Physics of Plasmas*, 2009, pp. 1–10. doi:10.1063/1.3056397.

[25] Goebel, D. M., Jameson, K. K., Watkins, R. M., Katz, I., and Mikellides, I. G., "Hollow cathode theory and experiment. I . Plasma characterization using fast miniature scanning probes," *Journal of Applied Physics*, Vol. 98, No. 11, 2005, p. 113302. doi:10.1063/1.2135417.

[26] Goebel, D. M., Jameson, K. K., Katz, I., and Mikellides, I. G., "Potential fluctuations and energetic ion production in hollow cathode discharges," *Physics of Plasmas*, Vol. 14, No. 10, 2007. doi:10.1063/1.2784460.

[27] Katz, I., and Mikellides, I. G., "Neutral gas free molecular flow algorithm including ionization and walls for use in plasma simulations," *Journal of Computational Physics*, Vol. 230, No. 4, 2011, pp. 1454–1464. doi:10.1016/j.jcp.2010.11.013.

[28] Mikellides, I. G., Katz, I., Goebel, D. M., and Jameson, K. K., "Evidence of nonclassical plasma transport in hollow cathodes for electric propulsion," *Journal of Applied Physics*, 2007, pp. 1–11. doi:10.1063/1.2710763.

[29] Jorns, B. A., Mikellides, I. G., and Goebel, D. M., "Ion acoustic turbulence in a 100-A LaB6 hollow cathode," *Physical Review E - Statistical, Nonlinear, and Soft Matter Physics*, Vol. 90, No. 6, 2014, pp. 1–10. doi:10.1103/PhysRevE.90.063106.

[30] Galeev, R. Z. S. A. A., *Nonlinear plasma theory*, W.A. Benjamin, Inc, New York, 1969.

[31] Mikellides, I. G., Katz, I., Jameson, K. K., and Goebel, D. M., "Numerical Simulations of a Hall Thruster Hollow Cathode Plasma," *30th International Electric Propulsion Conference*, 2007, pp. 1–12.

[32] Dushman, S., "Electron emission from metals," *Phys. Rev.*, Vol. 21, 1923, pp. 623–636. doi:10.1103/PhysRev.21.623.

[33] Mikellides, I. G., Goebel, D. M., Jorns, B. A., Polk, J. E., and Guerrero, P., "Numerical Simulations of the Partially Ionized Gas in a 100-A LaB 6 Hollow Cathode," *IEEE Transactions On Plasma Science*, Vol. 43, No. 1, 2015, pp. 173–184.

[34] García Rubiano, J., Mendoza, M., Gil, J., Rodriguez, R., Florido, R., Martel, P., and Mínguez, E., "Study of the radiative properties of plasma mixtures of interest for ICF chamber design using the ATMED code," *39th EPS Conference on Plasma Physics 2012, EPS 2012 and the 16th International Congress on Plasma Physics*, Vol. 3, 2012, p. P4.157.

[35] Rodriguez, R., Gil, J. M., Espinosa, G., Florido, R., Rubiano, J. G., Mendoza, M. A., Martel, P., Minguez, E., Symes, D. R., Hohenberger, M., and Smith, R. A., "Determination and analysis of plasma parameters for simulations of radiative blast waves launched in clusters of xenon and krypton," *Plasma Physics and Controlled Fusion*, Vol. 54, No. 4, 2012. doi:10.1088/0741-3335/54/4/045012.

[36] Desai, P. D., Chu, T. K., James, H. M., and Ho, C. Y., "Electrical Resistivity of Selected Elements," *Journal of Physical and Chemical Reference Data*, Vol. 13, No. 4, 1984, pp. 1069–1096. doi:10.1063/1.555723, URL `http://aip.scitation.org/doi/10.1063/1.555723`.

[37] Mikellides, I. G., Guerrero, P., Ortega, A. L., Goebel, D. M., and Polk, J. E., "Investigations of Spot-to-plume Mode Transition in a Hollow Cathode Discharge Using 2-D Axisymmetric Plasma Simulations," *54th AIAA/SAE/ASEE Joint Propulsion Conference, AIAA Propulsion and Energy Forum: American Institute of Aeronautics and Astronautics*, 2018, pp. 1–23.

[38] Shkarban, V. K. A. S. I., "Investigation of the Accelerated Ions Energy Accommodation Under Their Impingement with Solid Surfaces," *38th AIAA/ASME/SAE/ASEE Joint Propulsion Conference & Exhibit*, Vol. AIAA 2002-, 2002.